

Object Segmentation by Mining Cross-Modal Semantics

Zongwei Wu*
Computer Vision Lab, CAIDAS & IFI,
University of Wurzburg & University
of Burgundy, CNRS, ICB
Wurzburg, Germany
zongwei.wu.97@gmail.com

Jingjing Wang*
Anhui University of Science and
Technology
Huainan, China
wj9805@gmail.com

Zhuyun Zhou
University of Burgundy, CNRS, ICB
Dijon, France
zhuyun_zhou@etu.u-bourgogne.fr

Zhaochong An
CVL ETH Zurich
Zurich, Switzerland
1170801121@stu.hit.edu.cn

Qiuping Jiang
Ningbo University
Ningbo, China
jiangqiuping@nbu.edu.cn

Cédric Demonceaux
University of Burgundy, CNRS, ICB
Dijon, France
cedric.demonceaux@u-bourgogne.fr

Guolei Sun†
CVL ETH Zurich
Zurich, Switzerland
guolei.sun@vision.ee.ethz.ch

Radu Timofte
Computer Vision Lab, CAIDAS & IFI,
University of Wurzburg
Wurzburg, Germany
radu.timofte@uni-wuerzburg.de

ABSTRACT

Multi-sensor clues have shown promise for object segmentation, but inherent noise in each sensor, as well as the calibration error in practice, may bias the segmentation accuracy. In this paper, we propose a novel approach by mining the Cross-Modal Semantics to guide the fusion and decoding of multimodal features, with the aim of controlling the modal contribution based on relative entropy. We explore semantics among the multimodal inputs in two aspects: the modality-shared consistency and the modality-specific variation. Specifically, we propose a novel network, termed XMSNet, consisting of (1) all-round attentive fusion (AF), (2) coarse-to-fine decoder (CFD), and (3) cross-layer self-supervision. On the one hand, the AF block explicitly dissociates the shared and specific representation and learns to weight the modal contribution by adjusting the *proportion*, *region*, and *pattern*, depending upon the quality. On the other hand, our CFD initially decodes the shared feature and then refines the output through specificity-aware querying. Further, we enforce semantic consistency across the decoding layers to enable interaction across network hierarchies, improving feature discriminability. Exhaustive comparison on eleven datasets with depth or thermal clues, and on two challenging tasks, namely salient and

camouflage object segmentation, validate our effectiveness in terms of both performance and robustness. The source code is publicly available at <https://github.com/Zongwei97/XMSNet>.

CCS CONCEPTS

• **Computing methodologies** → **RGB-X object segmentation.**

KEYWORDS

RGB-X Object Segmentation, Cross-Modal Semantics, Robustness

ACM Reference Format:

Zongwei Wu, Jingjing Wang, Zhuyun Zhou, Zhaochong An, Qiuping Jiang, Cédric Demonceaux, Guolei Sun, and Radu Timofte. 2023. Object Segmentation by Mining Cross-Modal Semantics. In *Proceedings of the 31st ACM International Conference on Multimedia (MM '23)*, October 29–November 3, 2023, Ottawa, ON, Canada. ACM, New York, NY, USA, 10 pages. <https://doi.org/10.1145/3581783.3611970>

1 INTRODUCTION

Object segmentation is a fundamental task in computer vision, with applications in object grasping [16, 55], object tracking [24], and augmented reality [1, 6]. A number of learning-based methods [14, 20, 29, 38, 50, 65, 70] have shown plausible results in general settings. However, in practice, the objects of interest may be occluded by the foreground or even concealed from the background, making the segmentation task challenging.

Recently, there has been a growing interest in exploring multi-sensor, such as depth [25, 61] or thermal images [30, 51], for object segmentation, as different modalities can provide complementary clues to improve segmentation accuracy. In the ideal setting, the complement information is assumed to be perfect and well-aligned with the RGB input. In such a case, existing methods can offer impressive results [9, 49, 69]. However, this assumption does not always hold in practice. The additional modalities may contain misleading clues due to the inherent sensor noise [3, 48]. Moreover, as suggested in previous works [2, 66], even the state-of-the-art

*Both authors contributed equally to this research.

†Corresponding Author.

This research is financed in part by the Alexander von Humboldt Foundation and the Conseil Régional de Bourgogne-Franche-Comté. The authors thank the anonymous reviewers and ACs for their tremendous efforts and helpful comments.

Permission to make digital or hard copies of all or part of this work for personal or classroom use is granted without fee provided that copies are not made or distributed for profit or commercial advantage and that copies bear this notice and the full citation on the first page. Copyrights for components of this work owned by others than the author(s) must be honored. Abstracting with credit is permitted. To copy otherwise, or republish, to post on servers or to redistribute to lists, requires prior specific permission and/or a fee. Request permissions from [permissions@acm.org](https://www.acm.org/permissions).

MM '23, October 29–November 3, 2023, Ottawa, ON, Canada

© 2023 Copyright held by the owner/author(s). Publication rights licensed to ACM.

ACM ISBN 979-8-4007-0108-5/23/10...\$15.00

<https://doi.org/10.1145/3581783.3611970>

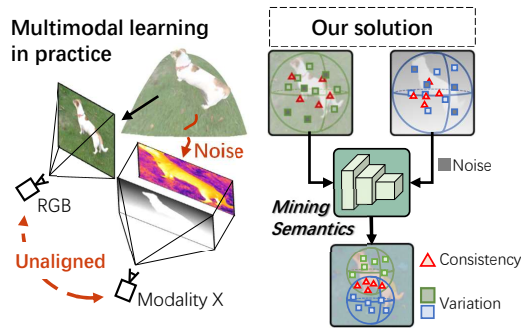


Figure 1: We consider the multimodal learning scenario in practice. Due to environmental factors and calibration bias, the complementary modality may be biased and not well-aligned with the RGB camera, making the fusion process challenging in a real-world setting. To deal with this practical issue, we propose a robust segmentation pipeline by mining the cross-modal semantics. Our method leads to preserved multimodal consistency, while pulling the modality-specific features in opposite directions to maximize the joint entropy, making our fusion design efficient and robust.

(SOTA) calibration methods cannot ensure a perfect alignment across sensors, making multimodal tasks challenging.

In the literature, there have been various fusion methods proposed for effectively merging multimodal clues [51, 56, 60, 61]. Many of them assume that the multi-sensor clues are heterogeneous, and can be directly merged to maximize the joint entropy [5, 18]. However, this design may have limitations, as it can also consider misleading noise as useful clues, leading to biased predictions. Therefore, a method that can effectively and robustly segment objects with any complementary clues is highly demanded.

In this work, we propose a novel approach for exploring the relationship between multi-sensor inputs by mining the cross-modal semantics, as shown in Figure 1. Our motivation stems from the observation that multimodal features, despite their modal specificity, inherently contain shared representations that are robust to measurements and/or calibration errors. Building upon this observation, we aim to leverage cross-modal consistency to guide the fusion of variant features that are specific to each input modality.

To achieve our objective, we first begin by explicitly decoupling the modality-shared and modality-specific features, treating them as separate entities during our modeling process. Drawing on the sensor denoising approaches suggested in previous works [35, 45], we adopt averaging as a popular method for mitigating the effects of shot, speckle, and ambient noise, which are known to impact accuracy. As such, we decompose each feature into two distinct components - mean and variance. The mean component of the feature map captures the shared consistency in a broader context, making it more robust to noise. Meanwhile, the variance component represents the relative modality-specific variation that may vary across modalities and are more susceptible to noise. Next, we employ an all-round attentive fusion strategy to process these two components. On one hand, based on the shared representation, we analyze the inner correlation between multimodal inputs and generate a learnable weight that balances the contributions of each modality to form the fused output. We expect less accurate depth or

infrared features to exhibit lower similarity compared to the RGB input, and consequently, contribute less to the fused output, and vice versa. On the other hand, considering the modality-specific features, which may also be noisy, we aim to determine which *regions* and *patterns* should be taken into account. By mining the cross-modal semantics, our fusion block enables a more effective feature modeling approach, retaining only the most informative modality-specific clues to maximize the joint entropy, while being robust to sensor noise.

Second, we also address the architectural aspect of our model. The U-shape skip connection has demonstrated outstanding results in object segmentation [8, 9, 44, 61, 78]. However, in the realm of multimodal fusion, existing approaches with conventional one-to-one correspondence may not fully exploit the potential of sensor fusion. To overcome this limitation, we propose a novel two-stage coarse-to-fine decoder. Initially, the feature map is decoded based on the shared semantics to estimate a rough object mask. Subsequently, the mask is further refined through cross-modal mining, resulting in a more discriminative output retaining the most informative clues from each input source.

Third, to improve the network learning process, we introduce constraints on the semantic consistency across the decoding layers. We postulate that despite the spatial variations depending upon the network depth, neighboring layers should still carry semantically related attributes. To achieve this goal, we gradually group the decoder outputs in pairs, forming low-, middle-, and high-level outputs, and then minimize the Kullback-Leibler divergence between them. This allows us to improve the stability and interpretability of feature decoding with minimal additional learning costs.

To conclude, our contributions can be summarized as follow:

- We propose a novel all-round attentive fusion by mining the cross-modal semantics in an explicit manner, which improves the accuracy and robustness of object segmentation.
- We introduce a two-stage decoder that combines convolution-based operations with cross-modal querying. The coarse-to-fine detection pipeline leads to a more discriminative output with a clearer contour.
- We further employ constraints on the semantic consistency across the decoding layers by minimizing the cross-level divergence, leading to improved learning stability and interpretability with minimal costs.
- Our network sets new SOTA records on multimodal object segmentation with both depth and infrared inputs. We also validate our robustness in challenging scenes with sub-optimal and/or misaligned inputs.

2 RELATED WORK

Object Segmentation with Depth Clues: Deep learning-based RGB-D networks [7, 13, 60, 85] have shown promising performance in object segmentation tasks by leveraging depth clues for improved scene understanding. Most existing works assume spatial alignment between RGB and depth images, based on which various fusion blocks have been proposed such as early fusion [13], middle fusion [28, 85], late fusion [8, 25], and output fusion [29, 84]. Nevertheless, such an assumption is not always the case in reality due to the sensor calibration error. To avoid the alignment issue, other works

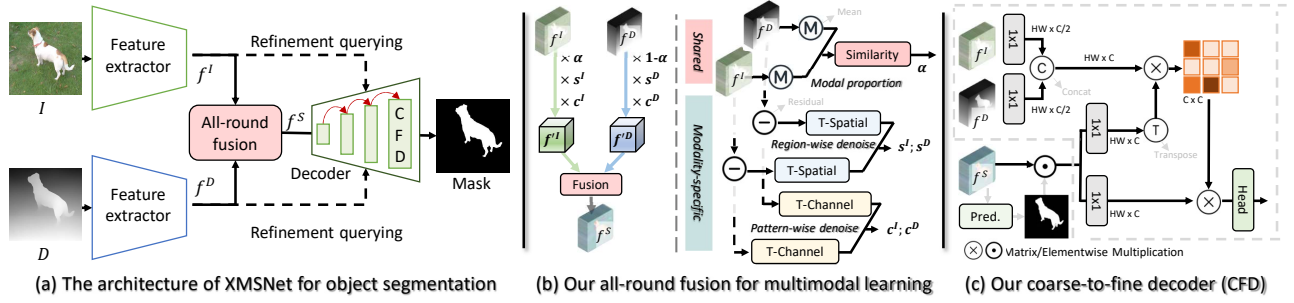


Figure 2: (a) Overall architecture of XMSNNet. Our network relies on standard backbones to extract RGB and depth features in a parallel manner. Then, the multimodal clues are attentively fused and decoded to segment the target object. **(b) Details on the fusion design.** We propose to leverage the semantics within the multimodal features before outputting the fused representation, by explicitly modeling the shared and specific components. **(c) Decoder pipeline.** We introduce a coarse-to-fine decoding strategy by first predicting the mask based on the shared representation, then refining it with modality-aware querying. By mining the cross-modal semantics, our network enables a more robust and efficient fusion architecture for object segmentation.

introduce depth-free modeling during testing by leveraging depth supervision during training [82, 83]. Sharing the same motivation, recent research proposes to generate pseudo-depth from RGB inputs [21, 62, 64, 68]. Nevertheless, in such a case, the quality of input data has been overlooked, and pseudo-depth may also suffer from domain gap issues. Several alternatives have proposed robust fusion strategies that consider input data quality, such as using attention mechanisms for feature calibration [19, 47, 63, 74]. However, these approaches do not explicitly differentiate modality-specific and shared clues during fusion, which can lead to inefficient RGB-D integration. In contrast, our work fully leverages consistency across multimodal inputs to merge modality-specific clues, resulting in a more robust and effective fusion design for object segmentation.

Object Segmentation with Thermal Clues: Recently, infrared images have gained research attention for object segmentation [17, 46, 54, 79, 86, 87], as they capture the thermal radiation emitted by objects, providing temperature information that can make objects distinguishable. Similar to RGB-D methods, learning-based RGB-T methods have achieved dominant performance in object segmentation. [51] suggests mining and modeling cross-modal interactions through channel attention, [88] proposes a lightweight model for real-time applications. [52] analyzes the RGB-T performance under the unaligned settings. [9] further studies the necessity of thermal clues based on the illuminance score. In contrast, our work computes the similarity between modality-shared features among RGB-T features and employs all-round fusion to fully benefit from multimodal inputs. By mining the cross-modal semantics, our network enables more robust and accurate object segmentation.

Challenging Scenes: In this paper, we additionally conduct experiments on challenging scenes with inaccurate depth and/or unaligned thermal inputs. To mimic inaccurate depth, we leverage off-the-shelf depth estimation methods following previous works [21, 62, 64, 68], which generate more realistic but noisy depth due to domain gap. We explicitly validate our method’s effectiveness on camouflage datasets [10, 64], which contain concealed scenes that are challenging for object segmentation. As for RGB-T inputs, since there is no existing thermal estimation method, we conduct experiments with unaligned inputs following [52]. The quantitative results validate the effectiveness and robustness of our method.

3 METHODOLOGY

For ease and brevity of reading, in this section, we take Depth as the auxiliary modality as an example, since the RGB-T model follows the same pipeline. Given an input image I with size $I \in \mathbb{R}^{3 \times H \times W}$, our objective is to segment the target object with the help of the depth clues D , which is resized to be the same resolution as I from the input side. As shown in Figure 2, I, D are fed into parallel encoders and output multi-scale encoded features F_i^I, F_i^D , where i stands for the number of encoder layers. At each scale, the encoded features are fed together into the all-round attentive fusion block (AF) to generate the shared output. After that, these features are later processed and refined by the coarse-to-fine decoder (CFD) to estimate the object’s location. To supervise the learning pipeline end-to-end, we leverage multi-scale supervision with the help of the ground truth mask G . Moreover, we explore the semantic consistency across different levels with respect to the network depth, which improves the network stability and interpretability.

3.1 All-Round Attentive Fusion

We observe that modality-shared features exhibit a strong correlation with scene semantics, suggesting a natural way to analyze cross-modal consistency. On the other hand, the residual part of the features may contain both discriminative modality-specific variations that contribute to segmentation and noise that hinders accurate predictions. Building upon this observation, we propose an all-round attentive fusion approach that mines the cross-modal semantics while respecting the inner consistency to maximize joint entropy and attenuate the impact of noise.

Adjusting Modal Proportion: Taking the encoded feature (f_i^I, f_i^D) of the i^{th} layer as an example, we first decompose it into two complementary components, i.e., the mean encodings (m_i^I, m_i^D) and the residual variance encoding (v_i^I, v_i^D) . The mean encodings are with shape $\mathbb{R}^{c \times 1 \times 1}$ and are obtained by performing global average pooling (GAP) on the input features, making the representation more robust to noise. Then, the mean encodings are fused together to generate the shared underlying features $m_s \in \mathbb{R}^{c \times 1 \times 1}$ of the scene. Mathematically, we have:

$$m_i^S = MLP(m_i^I \otimes m_i^D), \quad m_i^I = GAP(f_i^I), \quad m_i^D = GAP(f_i^D), \quad (1)$$

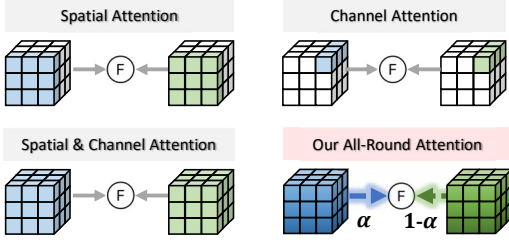


Figure 3: Fusion comparison. Attention mechanisms have been proven for multimodal fusion, such as spatial attention [63, 84], channel attention [19, 82], and both [76, 78]. However, existing works often directly compute the attention from the input features, without explicitly modeling the cross-modal semantics. Differently, we decompose each modality into shared and specific components and perform all-round fusion by adjusting the *proportion, region, and pattern*, depending upon the quality.

where MLP denotes multi-layer perceptron and \otimes is the matrix multiplication. Therefore, we can obtain the confidence score ($\alpha_i, 1-\alpha_i$) referring to the proportion of each modal contribution. Formally, we obtain α_i by computing the cosine similarity:

$$\alpha_i = \frac{a_i}{a_i + b_i}, \quad a_i = \text{cosine}(m_i^S, m_i^I), \quad b_i = \text{cosine}(m_i^S, m_i^D). \quad (2)$$

Region-wise Modeling: The variance encodings are with shape $\mathbb{R}^{c \times h \times w}$ and are obtained by the residual subtraction. They are supposed to contain valuable modality-specific clues but are also sensitive to noise. Therefore, we aim to preserve and enhance the most informative clues, while minimizing the inherent noisy response. To achieve this goal, we propose trio spatial attention (TSA) and trio channel attention (TCA) to improve the feature modeling *pattern-wise* and *region-wise*, respectively. Our TSA follows a hybrid design of “max-pooling + average-pooling + convolution”. The max-average branches contribute to preserving the effective and global clues, respectively, while the convolutional branch constrains network attention to local regions to alleviate ambiguity. After learning the spatial maps from each input, we enable cross-modal interaction by concatenation, and generate the final spatial-wise calibration maps (s_i^I, s_i^D) by convolution. Formally, we have:

$$\begin{aligned} s_i^I, s_i^D &= \text{chunk}(\text{CC}(\text{TSA}(v_i^I), \text{TSA}(v_i^D))), \\ s_i^I &= \sigma(s_i^I), \quad s_i^D = \sigma(s_i^D), \end{aligned} \quad (3)$$

where CC stands for concat-conv and σ is the sigmoid function.

Pattern-wise Modeling: As for channel dimension, our TCA follows the same philosophy by replacing the convolution with the gating function adopted from [72]. We obtain the channel-wise calibration maps (c_i^I, c_i^D) by:

$$\begin{aligned} c_i^I, c_i^D &= \text{chunk}(\text{CsC}(\text{TCA}(v_i^I), \text{TCA}(v_i^D))), \\ c_i^I &= \sigma(c_i^I), \quad c_i^D = \sigma(c_i^D), \end{aligned} \quad (4)$$

where CsC stands for concat-shuffle-conv. Finally, we can obtain the shared output f_i^S by:

$$\begin{aligned} f_i^I &= \alpha_i \cdot s_i^I \otimes c_i^I \otimes f_i^I, \quad f_i^D = (1 - \alpha_i) \cdot s_i^D \otimes c_i^D \otimes f_i^D, \\ f_i^S &= \text{Rearrange}(\text{MLP}(\text{Rearrange}(\text{Concat}(f_i^I, f_i^D)))) \end{aligned} \quad (5)$$

where MLP stands for the multi-layer perceptron with the required size arrangement. Starting from the second layer ($i > 1$), we merge the output f_i^S with the previous level output f_{i-1}^S with concat-conv.

3.2 Coarse-to-Fine Decoder

As a multimodal pipeline, the decoder aims to leverage both modality-specific and shared-learning representations to accurately generate the output. Many existing works [19, 63] are only based on the shared learning network, neglecting the rich modality-specific features for the decoder. Several recent models [84, 85] introduce triple decoders with both specific and shared networks, at the cost of increased learning complexity. In contrast, we propose a novel decoder that initially estimates the object’s location based on shared features and then refines it using our modality-aware querying to further mine the cross-modal semantics, yielding a lightweight yet efficient manner for object segmentation.

Initial Prediction: Our initial prediction block consists of a Local-Global Modeling (LGM) block, a Feature Merging (FM) block, and a prediction Head. The LGM block aims to improve the feature modeling with global and local awareness while being lightweight. Inspired by the success of inverted residual block from MobileNets [42], we first project the input feature map into a higher-dimension latent space by 1×1 convolution and then divide the projected feature into several subparts along the channel dimension. Each subpart is processed separately with maxpooling operation of different receptive fields. Our design shares the same motivation as PSPNet [81] and ASPP [71] that we all aim to leverage multi-scale global awareness. Differently, instead of using convolution, we only employ pooling operations which do not add extra learning parameters. The maxpooling operation can also contribute to preserving the most informative clues. We pad the feature map with respect to the pooling window so that the output resolution remains unchanged. Further, we employ a combination of depthwise separate convolution (DSCConv) to add locality into the network since fine-grained details are vital for accurate segmentation. Finally, the obtained feature is fed into a 1×1 convolution to enable information exchanges across channels and to reduce the dimension. Detailed feature flow can be found in Figure 4. Formally, let f_i^S be the input of LGM block of i^{th} decoding layer, the output LG_i is obtained by:

$$\begin{aligned} MP_1, MP_2, \dots, MP_N &= \text{MaxPooling}(\text{chunk}(\text{Conv}_{1 \times 1}(f_i^S))), \\ LG_i &= \text{Conv}_{1 \times 1}(\text{DSCConv}_{3 \times 3}(\text{Concat}(MP_1, MP_2, \dots, MP_N))). \end{aligned} \quad (6)$$

Aside from the LGM block, we propose an FM block that enables feature interaction between different decoding layers to benefit from the multi-granularity properties. As shown in Figure 4, the lower-resolution feature f_{i+1} is upsampled, multiplied with the higher-resolution feature LG_i , and fed into the MLP block to generate the initial feature f_i . When $i = 4$, i.e., the deepest layer, we replace the lower-resolution input of the FM block with the averaged feature. Finally, we employ the detection Head composed of one $\text{Conv}_{3 \times 3}$ and one $\text{Conv}_{1 \times 1}$, as shown in Figure 4, for the initial prediction p_i . Formally, we have:

$$\begin{aligned} f_i &= \text{Rearrange}(\text{MLP}(\text{Rearrange}(f_{i+1} \otimes LG_i))), \\ p_i &= \text{Head}(f_i), \end{aligned} \quad (7)$$

where Rearrange is the manipulation of the feature shape.

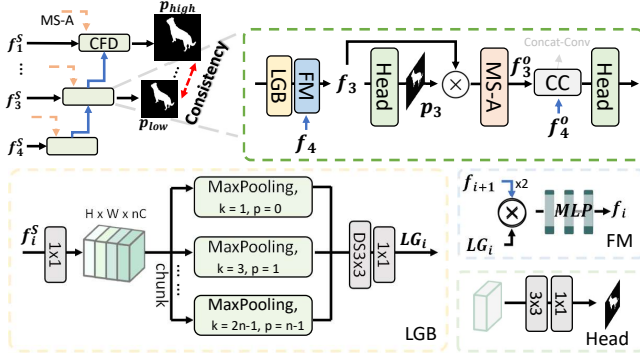


Figure 4: Our proposed coarse-to-fine decoder. Based on the shared representation, we first estimate the rough segmentation mask by employing wider receptive fields (LGB) and network hierarchies (FM). Then, the rough segmentation is refined with masked attention which aims to leverage the cross-modal semantics for improved discriminability.

Modality-Aware Querying: Based on the shared features, it is possible to obtain a rough but unprecise segmentation mask. Therefore, we propose a novel masked semantic mining attention, termed MS-A, with modality-aware querying. Our query is generated by mining the semantics across RGB and depth feature (f_i^I, f_i^D), while the key and value are computed and masked from the shared feature by $p_i \otimes f_i$. Formally, our MS-A can be formulated as:

$$\begin{aligned} Q &= \text{Rearrange}(\text{CC}(\text{Conv}_{1 \times 1}(f_i^I), \text{Conv}_{1 \times 1}(f_i^D))), \\ K &= \text{Rearrange}(\text{Conv}_{1 \times 1}(p_i \otimes f_i)), \\ V &= \text{Rearrange}(\text{Conv}_{1 \times 1}(p_i \otimes f_i)), \\ \text{MS-A}(Q, K, V) &= \text{softmax}\left(\frac{QK^T}{\sqrt{d_k}}\right)V, \end{aligned} \quad (8)$$

where Q, K, V stands for query, key, and value matrices. Our masked attention specifically focuses on the channel dimension for three reasons: (1) it requires very few learning parameters compared to other spatial counterparts [4, 32, 32, 59]; (2) we leverage modality-aware querying to mine the cross-modal semantics, making the attention map less sensitive to inherent sensor noise; (3) this design aligns with our goal that the prediction mask can only be refined but not enlarged, once again improving the robustness. With the help of our MS-A, we can output the refined feature map f_i^o by:

$$f_i^o = \text{MS-A}(Q, K, V) + p_i \otimes f_i. \quad (9)$$

3.3 Objective Function

Our XMSNet is end-to-end trainable and is only supervised by the GT mask G . Following previous works [63, 85], we adopt mixed objectives function \mathcal{L} consists of weighted binary cross-entropy loss \mathcal{L}^{wbce} and the IoU loss \mathcal{L}^{IoU} as follow:

$$\mathcal{L}(\cdot) = \mathcal{L}^{wbce}(\cdot) + \mathcal{L}^{IoU}(\cdot). \quad (10)$$

We first employ multi-scale loss \mathcal{L}^{ms} to supervise the initial predictions p_i from different decoding layers to fully benefit from the hierarchical information. We have:

$$\mathcal{L}^{ms} = \sum_{i=1}^4 \lambda_i \cdot \mathcal{L}(p_i, G), \quad (11)$$

where λ_i are the weighting hyperparameters.

Aside from this, we also leverage a multi-level loss \mathcal{L}^{ml} . Our assumption is that neighboring layers should carry closely-related attributes, making it possible to group decoded outputs in pairs, forming low-, middle-, and high-level outputs. Technically, taking the low-level output p_{low} as an example, we can obtain it by:

$$p_{low} = \text{Head}(f_{low}), \quad f_{low} = \text{CC}(f_4^o, f_3^o). \quad (12)$$

Then, the f_{low} is fused with the next layer output, gradually forming the middle-level output f_{mid} and high-level output f_{high} , from which we compute the refined masks p_{mid} and p_{high} , respectively. Mathematically, our multi-level loss \mathcal{L}^{ml} is formulated as:

$$\mathcal{L}^{ml} = \mathcal{L}(p_{low}, G) + \beta_1 \cdot \mathcal{L}(p_{mid}, G) + \beta_2 \cdot \mathcal{L}(p_{high}, G), \quad (13)$$

where β_1 and β_2 are the weighting parameters. Moreover, from a macroscopic view, there should exist a semantic consistency across different levels despite the resolution differences. Hence, we employ Kullback-Leibler divergence (KL) to force semantic consistency. Formally, our divergence loss \mathcal{L}^{div} becomes:

$$\begin{aligned} \mathcal{L}^{div} &= \mathcal{L}^{KL}(p_{low}, p_{mid}) + \mathcal{L}^{KL}(p_{mid}, p_{high}), \\ \mathcal{L}^{KL}(A, B) &= KL(A||B) + KL(B||A). \end{aligned} \quad (14)$$

Hence, our overall losses function \mathcal{L}^{all} becomes:

$$\mathcal{L}^{all} = \mathcal{L}^{ms} + \gamma_1 \cdot \mathcal{L}^{ml} + \gamma_2 \cdot \mathcal{L}^{div}. \quad (15)$$

where γ_1 and γ_2 are the weighting parameters. The ablation study on the hyperparameters can be found in the supplementary material.

4 EXPERIMENTS

4.1 Experimental Settings

Benchmark Datasets: We present experimental results on both RGB-D and RGB-T salient object detection (SOD) datasets to validate our effectiveness. For the RGB-D SOD task, we follow the standard protocol of previous works [12, 19, 63, 85] and select 1,485 samples from NJU2K [22] and 700 samples from NLPR [39] for training. We evaluate our model on four widely used RGB-D SOD datasets, including NLPR-Test [39], NJUK-Test [22], STERE [37], and SIP [11]. To analyze the robustness against noisy measurements, we also evaluate our model with pseudo-depth inputs [36, 41].

For the RGB-T SOD task, we follow the conventional train/val split as used in previous works [9, 18, 30, 54] and evaluate our method on three widely used RGB-T datasets: VT5000 [53], VT1000 [54], and VT821 [57]. To analyze the robustness against sensor misalignment, we also test on the biased datasets from [52].

In addition, we evaluate our method on the challenging task of camouflage object detection (COD), using pseudo-depth inputs, following previous works [36, 41, 64]. We use 3,040 images from COD10K [10] and 1,000 images from CAMO [23] for training, and test on four COD benchmark datasets: CAMO-Test [23], CHAM.[43], COD10K-Test [10], and NC4K [34].

Evaluation Metrics: We use four widely used evaluation metrics, namely Mean absolute error (M), max F-measure (F_m), S-measure (S_m), and E-measure (E_m), as commonly used in previous works [64, 85]. More details can be found in the supplementary material.

Implementation Details: Our model is implemented based on Pytorch with a V100 GPU. We chose pretrained PVT [59] as our

Table 1: Quantitative comparison on RGB-D SOD datasets with both GT depth and pseudo-depth. \uparrow (\downarrow) denotes that the higher (lower) is better. Bold denotes the best performance.

Public.	Dataset Metric	NLPR [39]				NJUK [22]				STERE [37]				SIP [11]			
		$M \downarrow$	$F_m \uparrow$	$S_m \uparrow$	$E_m \uparrow$	$M \downarrow$	$F_m \uparrow$	$S_m \uparrow$	$E_m \uparrow$	$M \downarrow$	$F_m \uparrow$	$S_m \uparrow$	$E_m \uparrow$	$M \downarrow$	$F_m \uparrow$	$S_m \uparrow$	$E_m \uparrow$
Oracle setting - Performance of Models Trained w/ GT Depth																	
<i>CVPR</i> ₂₁ [19]	DCF	.022	.918	.924	.958	.036	.922	.912	.946	.039	.911	.902	.940	.052	.899	.876	.916
<i>ICCV</i> ₂₁ [85]	SPNet	.021	.925	.927	.959	.028	.935	.925	.954	.037	.915	.907	.944	.043	.916	.894	.930
<i>MM</i> ₂₁ [33]	TriTrans	.020	.923	.928	.960	.030	.926	.920	.925	.033	.911	.908	.927	.043	.898	.886	.924
<i>ECCV</i> ₂₂ [84]	MVSNet	.022	.931	.930	.960	.036	.923	.912	.944	.036	.921	.913	.944	-	-	-	-
<i>ECCV</i> ₂₂ [25]	SPSN	.023	.917	.923	.956	.032	.927	.918	.949	.035	.909	.906	.941	.043	.910	.891	.932
<i>TIP</i> ₂₃ [61]	HiDANet	.021	.929	.930	.961	.029	.939	.926	.954	.035	.921	.911	.946	.043	.919	.892	.927
Ours	XMSNet	.018	.938	.936	.967	.025	.942	.931	.960	.026	.935	.927	.958	.032	.939	.913	.952
Practical setting - Performance of Models Trained w/o GT Depth																	
<i>ECCV</i> ₂₀ [12]	BBSNet	.023	.922	.923	.952	.037	.925	.915	.939	.037	.919	.914	.937	.053	.892	.875	.912
<i>MM</i> ₂₁ [80]	DFMNet	.027	.909	.914	.944	.046	.903	.895	.927	.042	.906	.903	.934	.067	.873	.850	.891
<i>TIP</i> ₂₂ [56]	DCMF	.027	.915	.921	.943	.044	.908	.903	.929	.041	.909	.907	.931	.067	.873	.853	.893
<i>CVPR</i> ₂₂ [20]	SegMAR	.024	.923	.920	.952	.036	.921	.909	.941	.037	.916	.907	.936	.052	.893	.872	.914
<i>CVPR</i> ₂₂ [38]	ZoomNet	.023	.916	.919	.944	.037	.926	.914	.940	.037	.918	.909	.938	.054	.891	.868	.909
Ours	XMSNet	.018	.929	.933	.964	.026	.941	.929	.959	.027	.934	.926	.955	.039	.926	.899	.936

Table 2: Quantitative comparison on RGB-T SOD datasets with both aligned and unaligned inputs.

Public.	Dataset Metric	VT5000 [53]				VT1000 [54]				VT821 [57]			
		$M \downarrow$	$F_m \uparrow$	$S_m \uparrow$	$E_m \uparrow$	$M \downarrow$	$F_m \uparrow$	$S_m \uparrow$	$E_m \uparrow$	$M \downarrow$	$F_m \uparrow$	$S_m \uparrow$	$E_m \uparrow$
Oracle setting - Performance of Models Trained w/ Aligned Thermal Inputs													
<i>TMM</i> ₂₂ [9]	TNet	.032	.895	.895	.932	.021	.937	.928	.957	.030	.903	.898	.928
<i>TCSV</i> ₂₂ [58]	CGFnet	.035	.886	.882	.923	.023	.933	.921	.955	.036	.881	.879	.916
<i>TIP</i> ₂₂ [52]	DCNet	.040	.848	.853	.906	.023	.918	.915	.953	.036	.848	.859	.911
<i>TIP</i> ₂₃ [88]	LSNet	.037	.871	.877	.917	.022	.930	.925	.954	.033	.870	.878	.915
<i>ICME</i> ₂₃ [30]	SSNet	.042	.845	.843	.894	.026	.918	.905	.945	.035	.867	.856	.896
Ours	XMSNet	.025	.909	.908	.949	.016	.942	.936	.968	.023	.913	.909	.944
Practical setting - Performance of Models Trained w/o Aligned Thermal Inputs													
<i>TIP</i> ₂₁ [51]	MIDD	.052	.841	.843	.889	.034	.906	.895	.934	.058	.835	.840	.882
<i>TCSV</i> ₂₁ [32]	SwinNet	.034	.876	.878	.932	.026	.919	.913	.954	.040	.860	.868	.912
<i>TIP</i> ₂₂ [52]	DCNet	.045	.833	.844	.906	.027	.899	.901	.949	.052	.824	.839	.897
<i>TMM</i> ₂₂ [9]	TNet	.043	.846	.856	.912	.031	.896	.894	.933	.044	.839	.855	.904
<i>TIP</i> ₂₃ [88]	LSNet	.049	.810	.828	.898	.035	.876	.883	.933	.047	.799	.829	.894
Ours	XMSNet	.028	.895	.897	.943	.018	.935	.928	.962	.029	.889	.892	.933

backbone. Detailed comparisons with different backbones can be found in Table 4. The input dimension is set to 384×384 . The Adam algorithm is adopted as an optimizer. The initial learning rate is set to $1e-4$ which is divided by 10 every 60 epochs. Follow [85], we use common data augmentation operations. The network is trained for 200 epochs with the same hyperparameters settings for each task.

4.2 Comparison with RGB-D/T Inputs

Quantitative Comparison w/ Ground Truth Depth: We present our performance on RGB-D SOD benchmarks in Table 1. When using ground truth depth, our method achieves significantly superior performance over all the counterparts by a large margin. The superior performance validates the effectiveness of our XMSNet.

Quantitative Comparison w/o Ground Truth Depth: We also evaluate our method by replacing GT depth with source-free depth. Following previous works [64, 68], we generate pseudo-depth from the input RGB image [40, 41]. We retrain three RGB-D methods, i.e., BBSNet [12], DFMNet [80], and DCMF [56], as well as two state-of-the-art segmentation methods with RGB-only inputs, i.e., SegMAR [20] and ZoomNet [38]. It can be seen that most existing RGB-D methods fail to perform accurately when dealing with

pseudo-depth, and the RGB-only methods provide reasonable but far from satisfactory performance. In contrast, our XMSNet still leverages pseudo-depth clues and provides promising results. This is attributed to our design of mining cross-modal semantics, which eliminates misleading noise in the depth map, yielding superior robustness and efficiency compared to all other counterparts.

Quantitative Comparison w/ Aligned Thermal Image: Table 2 displays the performance of our method on RGB-T SOD benchmarks, where our approach significantly outperforms all counterparts on every dataset and metric.

Quantitative Comparison w/o Aligned Thermal Image: We conducted experiments on the unaligned datasets [52], where misalignment was generated through random spatial affine transformation. The results are presented in Table 2. Our proposed method achieved outstanding performance, outperforming DCNet [52], which introduced a specific modality alignment module. Our approach highlights the significance of mining cross-modal semantics, which leads to stable performance. While SwinNet [32], the second-best approach, leverages transformer attention for feature fusion, it only aims to maximize joint entropy and may classify unaligned features as useful modality-specific clues. In contrast, our approach

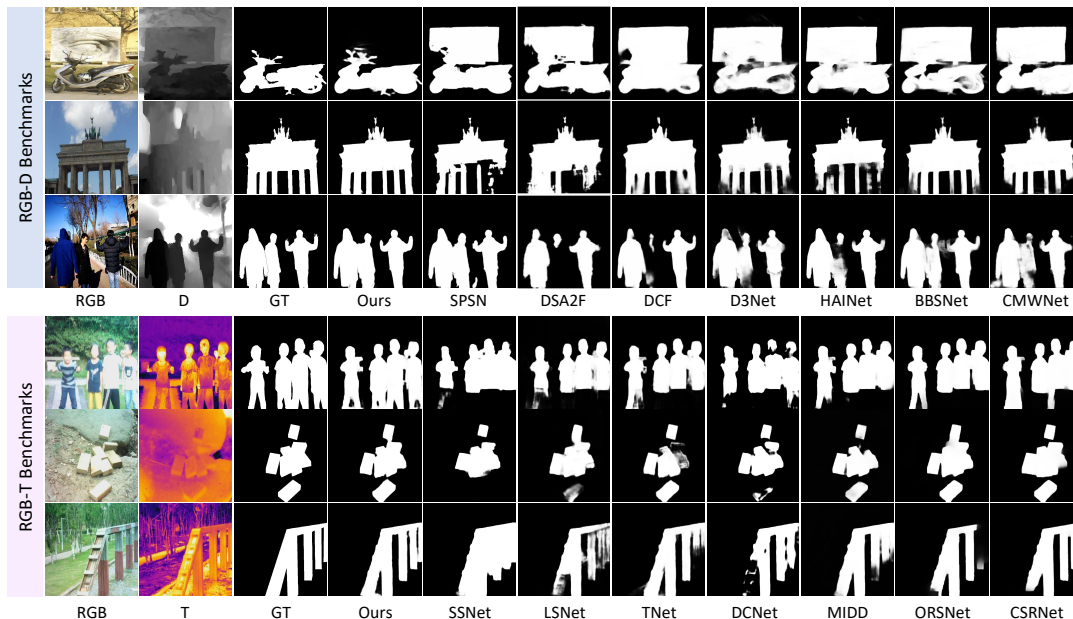


Figure 5: Qualitative comparison on RGB-D/T SOD benchmarks. Our network can efficiently leverage both visual and additional clues from supporting modality to accurately segment the target object which is closer to the ground truth.

Table 3: Quantitative comparison with pseudo-depth on challenging COD datasets

Public.	Dataset Metric	CAMO [23]				CHAM. [43]				COD10K [10]				NC4K [34]			
		$M \downarrow$	$F_m \uparrow$	$S_m \uparrow$	$E_m \uparrow$	$M \downarrow$	$F_m \uparrow$	$S_m \uparrow$	$E_m \uparrow$	$M \downarrow$	$F_m \uparrow$	$S_m \uparrow$	$E_m \uparrow$	$M \downarrow$	$F_m \uparrow$	$S_m \uparrow$	$E_m \uparrow$
Performance of RGB COD Models																	
<i>MM</i> ₂₁ [75]	UJSC	.072	.812	.800	.861	.030	.874	.891	.948	.035	.761	.808	.886	.047	.838	.841	.900
<i>CVPR</i> ₂₁ [26]	SegMAR	.080	.799	.794	.857	.032	.871	.887	.935	.039	.750	.799	.876	.050	.828	.836	.893
<i>CVPR</i> ₂₂ [20]	ZoomNet	.074	.818	.801	.858	.033	.829	.859	.915	.034	.771	.808	.872	.045	.841	.843	.893
<i>CVPR</i> ₂₂ [38]	FEDER	.071	.823	.802	.868	.029	.874	.886	.948	-	-	-	-	.044	.852	.847	.909
<i>CVPR</i> ₂₃ [14]																	
Performance of RGB-D COD Models																	
<i>MM</i> ₂₁ [75]	CDINet	.100	.638	.732	.766	.036	.787	.879	.903	.044	.610	.778	.821	.067	.697	.793	.830
<i>CVPR</i> ₂₁ [19]	DCF	.089	.724	.749	.834	.037	.821	.850	.923	.040	.685	.766	.864	.061	.765	.791	.878
<i>TIP</i> ₂₁ [27]	HAINet	.084	.782	.760	.829	.028	.876	.876	.942	.049	.735	.781	.865	.057	.809	.804	.872
<i>ICCV</i> ₂₁ [76]	CMINet	.087	.798	.782	.827	.032	.881	.891	.930	.039	.768	.811	.868	.053	.832	.839	.888
<i>ICCV</i> ₂₁ [85]	SPNet	.083	.807	.783	.831	.033	.872	.888	.930	.037	.776	.808	.869	.054	.828	.825	.874
<i>TIP</i> ₂₂ [56]	DCMF	.115	.737	.728	.757	.059	.807	.830	.853	.063	.679	.748	.776	.077	.782	.794	.820
<i>ECCV</i> ₂₂ [25]	SPSN	.084	.782	.773	.829	.032	.866	.887	.932	.042	.727	.789	.854	.059	.803	.813	.867
Ours	XMSNet	.048	.871	.864	.923	.025	.895	.904	.950	.024	.828	.861	.927	.034	.877	.879	.933

explicitly models cross-modal consistency to guide multimodal fusion, resulting in better robustness against misalignment.

Qualitative Comparison: We provide qualitative results on RGB-D/T benchmark datasets in Figure 5. Our method efficiently distinguishes misleading and useful clues during multimodal fusion, either for RGB-D or RGB-T inputs.

4.3 Performance on the Camouflaged Scenes

Camouflaged object detection (COD) is a challenging task that has recently drawn great research attention [10, 77]. As the object is concealed from the background, the COD task is inherently difficult. While multimodal clues such as depth have been shown to be useful for object segmentation [64, 67], the lack of ground truth inputs, such as the depth map, makes it necessary to use off-the-shelf depth estimation methods, which introduces noise due to the domain gap. As shown in Table 3, existing RGB-D methods with pseudo-depth perform worse than RGB-only methods. However, our method outperforms both RGB-D and RGB-only methods in all

Table 4: Quantitative results based on different backbones.

Backbone	Dataset	Model	$M \downarrow$	$F_m \uparrow$	$S_m \uparrow$	$E_m \uparrow$
ResNet [15]	SIP [11]	C2DFNet [78]	.053	.894	.782	.911
		Ours	.036	.920	.902	.942
ConvNext [31]	CHAM. [43]	CamoFormer [73]	.024	.886	.901	.954
		Ours	.021	.899	.913	.970
PVT [59]	VT821 [57]	MTFNet[4]	.026	.906	.905	.938
		Ours	.023	.913	.909	.944

COD benchmarks, demonstrating our ability to efficiently leverage pseudo-depth despite several noisy representations. Qualitative comparisons can be found in the supplementary material.

4.4 Ablation Study

Different Backbones: We present in Table 4 our performance with different backbones such as (R) ResNet [15], (C) ConvNext [31], and (P) PVT [59]. Our model outperforms all the counterparts with the same backbone, validating our effectiveness. The comparison of the model sizes can be found in Figure 6, where our (R), (C), and (P) variants require 233MB, 727MB, and 670MB, respectively. It

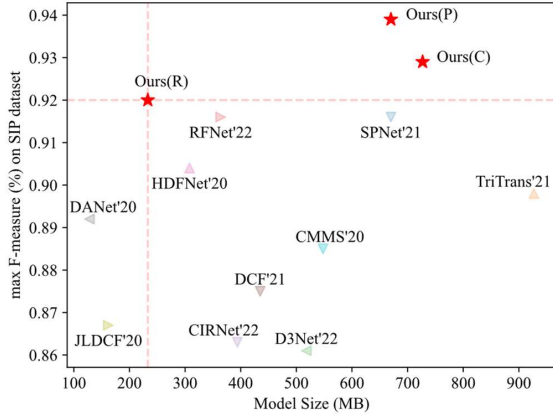


Figure 6: Model size comparison. Our networks lead to the best trade-off between efficiency and performance.

Table 5: Key component analysis.

AF	Pred + L_{ms}	MS-A + L_{div}	STERE [37]				SIP [11]			
			$M \downarrow$	$F_m \uparrow$	$S_m \uparrow$	$E_m \uparrow$	$M \downarrow$	$F_m \uparrow$	$S_m \uparrow$	$E_m \uparrow$
Component Ablation Study										
-	-	-	.042	.903	.894	.933	.048	.901	.882	.922
✓	-	-	.036	.919	.910	.943	.042	.911	.893	.930
✓	✓	-	.035	.920	.910	.942	.041	.911	.895	.932
✓	✓	✓	.032	.928	.915	.948	.036	.920	.902	.942
Replacing Our Component with SOTA Counterparts										
AF → RFNet [63]			.035	.919	.911	.942	.045	.907	.887	.923
AF → SPNet [85]			.035	.918	.910	.943	.047	.904	.882	.918
MS-A → CamoFormer [73]			.035	.922	.914	.942	.041	.912	.895	.931

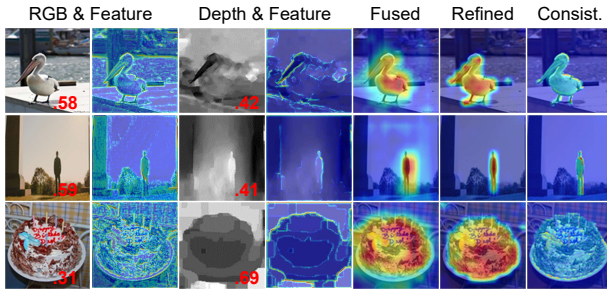


Figure 7: Feature visualization. Red value denotes the modal contribution. Please, zoom in for more details.

can be seen that our network with ResNet backbone has already achieved the SOTA performance with a very competitive model size. Deeper backbones (C/P) further boost our performance. The full performances can be found in the supplementary material. In the following ablation studies, we use ResNet as the backbone.

Key Component Analysis: The contribution of each proposed block is presented in Table 5. Gradually adding our proposed block leads to improved performance. To enhance our analysis, we replaced fusion and masked attention components with the SOTA counterparts [63, 73, 85]. The results demonstrate that such replacements resulted in a deterioration of performance, further confirming the effectiveness of our proposed methods. For a more comprehensive understanding of each proposed block’s contribution, we provide visualizations of our encoded, fused, refined, and consistency-constrained features in Figure 7.

Ablation Study on the Fusion: We present a detailed study on the fusion block, comprising trio spatial attention (TSA), trio channel

Table 6: Ablation study on the proposed fusion block.

TSA	TCA	α	STERE [37]				SIP [11]			
			$M \downarrow$	$F_m \uparrow$	$S_m \uparrow$	$E_m \uparrow$	$M \downarrow$	$F_m \uparrow$	$S_m \uparrow$	$E_m \uparrow$
Component Ablation Study										
-	-	-	.037	.918	.909	.939	.049	.901	.880	.916
✓	-	-	.033	.923	.914	.947	.045	.908	.887	.923
-	✓	-	.033	.922	.914	.948	.039	.914	.898	.934
-	-	✓	.033	.921	.913	.947	.040	.912	.895	.932
✓	-	✓	.033	.924	.915	.947	.040	.912	.897	.934
✓	✓	-	.034	.919	.912	.945	.038	.917	.900	.938
✓	✓	✓	.032	.928	.915	.948	.036	.920	.902	.942
Replacing TSA/TCA with Basic Component										
TSA → Max			.034	.920	.911	.945	.047	.906	.886	.920
TSA → Mean			.034	.921	.910	.945	.046	.906	.885	.921
TSA → Conv			.033	.924	.914	.946	.043	.907	.891	.928
TCA → GCT			.034	.920	.911	.944	.042	.910	.890	.929
TCA → Mean			.034	.919	.909	.944	.042	.913	.894	.929
TCA → Max			.034	.921	.914	.945	.043	.908	.891	.929

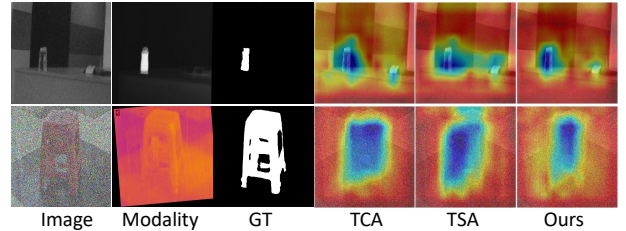


Figure 8: Attention Visualization under Unaligned Setting.

attention (TCA), and the proportion α , in Table 6. By gradually removing other components, we validate the effectiveness of each element, with our full fusion design achieving the best performance. Additionally, we conducted a comprehensive analysis by replacing the trio attention with each basic attention branch. The observed deteriorated performance highlights the significance of our complete trio branches attention design. For a better understanding of our fusion block’s functionality, we provide attention visualizations in Figure 8. When dealing with unaligned input, our TSA leverages global clues, such as shape and contour, while the TCA focuses on feature alignment across modalities.

Overall Modal Contribution: During testing on the RGB-X SOD dataset, consisting of 2729 RGB-D samples and 4321 RGB-T samples, we observed that RGB features were assigned higher weights in 1858 images (68.1% of the cases) for RGB-D inputs, and 3407 images (78.8% of the cases) for RGB-T inputs. This result confirms our initial hypothesis that depth or thermal clues may contain noise or misalignment compared to RGB inputs, and hence should generally contribute less to the shared output.

5 CONCLUSION

We demonstrate a successful case of mining cross-modal semantics for object segmentation. In this paper, we leverage the modality-shared consistency to guide the fusion of modality-specific variation, making the fusion design more robust to sensor noise and misalignment. Further, we design a coarse-to-fine decoder that fully benefits from the multimodal clues to strengthen the feature discriminability. Finally, we add restrictions on the decoded outputs to ensure semantic consistency across different layers, yielding a simple yet efficient manner to employ the network hierarchies. Exhaustive experiments on RGB-D and RGB-T SOD and COD benchmarks, with both GT and inferior inputs, validate the effectiveness, generalizing, and robustness of our XMSNet.

REFERENCES

- [1] Haley Adams, Jeanine Stefanucci, Sarah Creem-Regehr, and Bobby Bodenheimer. 2022. Depth perception in augmented reality: The effects of display, shadow, and position. In *IEEE VR*. IEEE.
- [2] Xuyang Bai, Zeyu Hu, Xinge Zhu, Qingqiu Huang, Yilun Chen, Hongbo Fu, and Chiew-Lan Tai. 2022. Transfusion: Robust lidar-camera fusion for 3d object detection with transformers. In *IEEE/CVF CVPR*.
- [3] Helmut Budzier and Gerald Gerlach. 2011. *Thermal infrared sensors: theory, optimisation and practice*. John Wiley & Sons.
- [4] Gang Chen, Feng Shao, Xiongli Chai, Hangwei Chen, Qiuping Jiang, Xiangchao Meng, and Yo-Sung Ho. 2022. Modality-Induced Transfer-Fusion Network for RGB-D and RGB-T Salient Object Detection. *IEEE TCSVT* (2022).
- [5] Qian Chen, Zhenxi Zhang, Yanye Lu, Keren Fu, and Qijun Zhao. 2022. 3-D Convolutional Neural Networks for RGB-D Salient Object Detection and Beyond. *IEEE TNNLS* (2022).
- [6] Kelvin Cheng, Kensuke Koda, and Soh Masuko. 2022. Reimagining the Stadium Spectator Experience using Augmented Reality and Visual Positioning System. In *IEEE ISMAR-Adjunct*. IEEE.
- [7] Xiaolong Cheng, Xuan Zheng, Jialun Pei, He Tang, Zehua Lyu, and Chuanbo Chen. 2022. Depth-induced Gap-reducing Network for RGB-D Salient Object Detection: An Interaction, Guidance and Refinement Approach. *IEEE TMM* (2022).
- [8] Runmin Cong, Qinwei Lin, Chen Zhang, Chongyi Li, Xiaochun Cao, Qingming Huang, and Yao Zhao. 2022. CIR-Net: Cross-modality Interaction and Refinement for RGB-D Salient Object Detection. *IEEE TIP* (2022).
- [9] Runmin Cong, Kepu Zhang, Chen Zhang, Feng Zheng, Yao Zhao, Qingming Huang, and Sam Kwong. 2022. Does thermal really always matter for RGB-T salient object detection? *IEEE TMM* (2022).
- [10] Deng-Ping Fan, Ge-Peng Ji, Guolei Sun, Ming-Ming Cheng, Jianbing Shen, and Ling Shao. 2020. Camouflaged object detection. In *IEEE CVPR*.
- [11] Deng-Ping Fan, Zheng Lin, Zhao Zhang, Menglong Zhu, and Ming-Ming Cheng. 2021. Rethinking RGB-D salient object detection: Models, datasets, and large-scale benchmarks. *IEEE TNNLS* 32, 5 (2021), 2075–2089.
- [12] Deng-Ping Fan, Yingjie Zhai, Ali Borji, Jufeng Yang, and Ling Shao. 2020. BBS-Net: RGB-D salient object detection with a bifurcated backbone strategy network. In *ECCV*.
- [13] Keren Fu, Deng-Ping Fan, Ge-Peng Ji, and Qijun Zhao. 2020. JL-DCF: Joint learning and densely-cooperative fusion framework for RGB-D salient object detection. In *IEEE CVPR*.
- [14] Chunming He, Kai Li, Yachao Zhang, Longxiang Tang, Yulun Zhang, Zhenhua Guo, and Xiu Li. 2023. Camouflaged Object Detection with Feature Decomposition and Edge Reconstruction. In *IEEE CVPR*.
- [15] Kaiming He, Xiangyu Zhang, Shaoqing Ren, and Jian Sun. 2016. Deep residual learning for image recognition. In *IEEE CVPR*.
- [16] Yisheng He, Haibin Huang, Haoqiang Fan, Qifeng Chen, and Jian Sun. 2021. Ffb6d: A full flow bidirectional fusion network for 6d pose estimation. In *IEEE CVPR*.
- [17] Dong Huo, Jian Wang, Yiming Qian, and Yee-Hong Yang. 2023. Glass segmentation with RGB-thermal image pairs. *IEEE TTP* 32 (2023), 1911–1926.
- [18] Fushuo Huo, Xuegui Zhu, Qian Zhang, Ziming Liu, and Wenchao Yu. 2022. Real-time one-stream semantic-guided refinement network for RGB-Thermal salient object detection. *IEEE TIM* 71 (2022), 1–12.
- [19] Wei Ji, Jingjing Li, Shuang Yu, Miao Zhang, Yongri Piao, Shunyu Yao, Qi Bi, Kai Ma, Yefeng Zheng, Huchuan Lu, et al. 2021. Calibrated RGB-D Salient Object Detection. In *IEEE CVPR*.
- [20] Qi Jia, Shuilian Yao, Yu Liu, Xin Fan, Risheng Liu, and Zhongxuan Luo. 2022. Segment, Magnify and Reiterate: Detecting Camouflaged Objects the Hard Way. In *IEEE CVPR*.
- [21] Wen-Da Jin, Jun Xu, Qi Han, Yi Zhang, and Ming-Ming Cheng. 2021. CDNet: Complementary depth network for RGB-D salient object detection. *IEEE TIP* 30 (2021), 3376–3390.
- [22] Ran Ju, Ling Ge, Wenjing Geng, Tongwei Ren, and Gangshan Wu. 2014. Depth saliency based on anisotropic center-surround difference. In *IEEE ICIP*.
- [23] Trung-Nghia Le, Tam V Nguyen, Zhongliang Nie, Minh-Triet Tran, and Akihiro Sugimoto. 2019. Anabranh network for camouflaged object segmentation. *CVIU* 184 (2019), 45–56.
- [24] Hyemin Lee and Daijin Kim. 2018. Salient region-based online object tracking. In *WACV*.
- [25] Minhyeok Lee, Chaewon Park, Suhwan Cho, and Sangyoung Lee. 2022. SPNS: Superpixel Prototype Sampling Network for RGB-D Salient Object Detection. In *ECCV*.
- [26] Aixuan Li, Jing Zhang, Yunqiu Lv, Bowen Liu, Tong Zhang, and Yuchao Dai. 2021. Uncertainty-aware joint salient object and camouflaged object detection. In *IEEE CVPR*.
- [27] Gongyang Li, Zhi Liu, Minyu Chen, Zhen Bai, Weisi Lin, and Haibin Ling. 2021. Hierarchical Alternate Interaction Network for RGB-D Salient Object Detection. *IEEE TIP* 30 (2021), 3528–3542.
- [28] Gongyang Li, Zhi Liu, Linwei Ye, Yang Wang, and Haibin Ling. 2020. Cross-modal weighting network for RGB-D salient object detection. In *ECCV*.
- [29] Jia Li, Shengye Qiao, Zhirui Zhao, Chenxi Xie, Xiaowu Chen, and Changqun Xia. 2023. Rethinking Lightweight Salient Object Detection via Network Depth-Width Tradeoff. *arXiv preprint arXiv:2301.06679* (2023).
- [30] Zhengyi Liu, Xiaoshen Huang, Guanghui Zhang, Xianyong Fang, Linbo Wang, and Bin Tang. 2023. Scribble-Supervised RGB-T Salient Object Detection. *arXiv preprint arXiv:2303.09733* (2023).
- [31] Zhuang Liu, Hanzi Mao, Chao-Yuan Wu, Christoph Feichtenhofer, Trevor Darrell, and Saining Xie. 2022. A convnet for the 2020s. In *IEEE/CVF CVPR*.
- [32] Zhengyi Liu, Yacheng Tan, Qian He, and Yun Xiao. 2021. SwinNet: Swin transformer drives edge-aware RGB-D and RGB-T salient object detection. *IEEE TCSVT* 32, 7 (2021), 4486–4497.
- [33] Zhengyi Liu, Wang Yuan, Zhengzheng Tu, Yun Xiao, and Bin Tang. 2021. Tri-TransNet: RGB-D Salient Object Detection with a Triplet Transformer Embedding Network. *ACM MM* (2021).
- [34] Yunqiu Lv, Jing Zhang, Yuchao Dai, Aixuan Li, Bowen Liu, Nick Barnes, and Deng-Ping Fan. 2021. Simultaneously localize, segment and rank the camouflaged objects. In *IEEE CVPR*.
- [35] Christopher A Metzler, Arian Maleki, and Richard G Baraniuk. 2016. From denoising to compressed sensing. *IEEE TIT* 62, 9 (2016), 5117–5144.
- [36] S Mahdi H Miangoleh, Sebastian Dille, Long Mai, Sylvain Paris, and Yagiz Aksoy. 2021. Boosting monocular depth estimation models to high-resolution via content-adaptive multi-resolution merging. In *IEEE CVPR*.
- [37] Yuzhen Niu, Yujie Geng, Xueqing Li, and Feng Liu. 2012. Leveraging stereopsis for saliency analysis. In *IEEE CVPR*.
- [38] Youwei Pang, Xiaoqi Zhao, Tian-Zhu Xiang, Lihe Zhang, and Huchuan Lu. 2022. Zoom in and Out: A Mixed-Scale Triplet Network for Camouflaged Object Detection. In *IEEE CVPR*.
- [39] Houwen Peng, Bing Li, Weihua Xiong, Weiming Hu, and Rongrong Ji. 2014. RGBD salient object detection: a benchmark and algorithms. In *ECCV*.
- [40] René Ranftl, Alexey Bochkovskiy, and Vladlen Koltun. 2021. Vision transformers for dense prediction. In *IEEE ICCV*.
- [41] René Ranftl, Katrin Lasinger, David Hafner, Konrad Schindler, and Vladlen Koltun. 2022. Towards robust monocular depth estimation: Mixing datasets for zero-shot cross-dataset transfer. *IEEE TPAMI* 44, 3 (2022), 1623–1637.
- [42] Mark Sandler, Andrew Howard, Menglong Zhu, Andrey Zhmoginov, and Liang-Chieh Chen. 2018. Mobilenetv2: Inverted residuals and linear bottlenecks. In *IEEE CVPR*.
- [43] Przemyslaw Skurowski, Hassan Abdulameer, J Błaszczyk, Tomasz Depta, Adam Kornacki, and P Koziel. 2018. Animal camouflage analysis: Chameleon database. *Unpublished manuscript* 2, 6 (2018), 7.
- [44] Mengke Song, Wenfeng Song, Guowei Yang, and Chenglizhao Chen. 2022. Improving RGB-D Salient Object Detection via Modality-Aware Decoder. *IEEE TIP* 31 (2022), 6124–6138.
- [45] Qingkun Song, Li Ma, JianKun Cao, and Xiao Han. 2015. Image denoising based on mean filter and wavelet transform. In *AITS*.
- [46] Fan Sun, Wujie Zhou, Lv Ye, and Lu Yu. 2022. Hierarchical decoding network based on swin transformer for detecting salient objects in RGB-T images. *IEEE SPL* 29 (2022), 1714–1718.
- [47] Peng Sun, Wenhui Zhang, Huanyu Wang, Songyuan Li, and Xi Li. 2021. Deep RGB-D Saliency Detection with Depth-Sensitive Attention and Automatic Multi-Modal Fusion. In *IEEE CVPR*.
- [48] Chris Sweeney, Greg Izatt, and Russ Tedrake. 2019. A supervised approach to predicting noise in depth images. In *ICRA*.
- [49] Bin Tang, Zhengyi Liu, Yacheng Tan, and Qian He. 2023. HRTransNet: HRFormer-Driven Two-Modality Salient Object Detection. *IEEE TCSVT* 33, 2 (2023), 728–742. <https://doi.org/10.1109/TCSVT.2022.3202563>
- [50] Lv Tang, Bo Li, Yijie Zhong, Shouhong Ding, and Mofei Song. 2021. Disentangled high quality salient object detection. In *IEEE/CVF ICCV*.
- [51] Zhengzheng Tu, Zhun Li, Chenglong Li, Yang Lang, and Jin Tang. 2021. Multi-interactive dual-decoder for RGB-thermal salient object detection. *IEEE TIP* 30 (2021), 5678–5691.
- [52] Zhengzheng Tu, Zhun Li, Chenglong Li, and Jin Tang. 2022. Weakly alignment-free RGBT salient object detection with deep correlation network. *IEEE TIP* 31 (2022), 3752–3764.
- [53] Zhengzheng Tu, Yan Ma, Zhun Li, Chenglong Li, Jieming Xu, and Yongtao Liu. 2022. RGBT salient object detection: A large-scale dataset and benchmark. *IEEE TMM* (2022).
- [54] Zhengzheng Tu, Tian Xia, Chenglong Li, Xiaoxiao Wang, Yan Ma, and Jin Tang. 2019. RGB-T image saliency detection via collaborative graph learning. *IEEE TMM* 22, 1 (2019), 160–173.
- [55] Chen Wang, Danfei Xu, Yuke Zhu, Roberto Martín-Martín, Cewu Lu, Li Fei-Fei, and Silvio Savarese. 2019. Densefusion: 6d object pose estimation by iterative dense fusion. In *IEEE CVPR*.
- [56] Fengyun Wang, Jinshan Pan, Shoukun Xu, and Jinhui Tang. 2022. Learning Discriminative Cross-Modality Features for RGB-D Saliency Detection. *IEEE TIP* 31 (2022), 1285–1297.

- [57] Guizhao Wang, Chenglong Li, Yunpeng Ma, Aihua Zheng, Jin Tang, and Bin Luo. 2018. RGB-T saliency detection benchmark: Dataset, baselines, analysis and a novel approach. In *IGTA*. Springer.
- [58] Jie Wang, Kechen Song, Yanqi Bao, Liming Huang, and Yunhui Yan. 2022. CGFNet: Cross-Guided Fusion Network for RGB-T Salient Object Detection. *IEEE TCSVT* 32, 5 (2022), 2949–2961. <https://doi.org/10.1109/TCSVT.2021.3099120>
- [59] Wenhai Wang, Enze Xie, Xiang Li, Deng-Ping Fan, Kaitao Song, Ding Liang, Tong Lu, Ping Luo, and Ling Shao. 2022. Pvt v2: Improved baselines with pyramid vision transformer. *CVMJ* 8, 3 (2022), 415–424.
- [60] Hongfa Wen, Chenggang Yan, Xiaofei Zhou, Runmin Cong, Yaoqi Sun, Bolun Zheng, Jiyong Zhang, Yongjun Bao, and Guiguang Ding. 2021. Dynamic selective network for RGB-D salient object detection. *TIP* 30 (2021), 9179–9192.
- [61] Zongwei Wu, Guillaume Allibert, Fabrice Meriaudeau, Chao Ma, and Cédric Demonceaux. 2023. HiDAnet: RGB-D Salient Object Detection via Hierarchical Depth Awareness. *IEEE TIP* 32 (2023), 2160–2173. <https://doi.org/10.1109/TIP.2023.3263111>
- [62] Zongwei Wu, Guillaume Allibert, Christophe Stolz, Chao Ma, and Cédric Demonceaux. 2021. Modality-Guided Subnetwork for Salient Object Detection. In *3DV*.
- [63] Zongwei Wu, Shriarulmozhiarman Gobichettipalayam, Brahim Tamadazte, Guillaume Allibert, Danda Pani Paudel, and Cédric Demonceaux. 2022. Robust RGB-D Fusion for Saliency Detection. In *3DV*.
- [64] Zongwei Wu, Danda Pani Paudel, Deng-Ping Fan, Jingjing Wang, Shuo Wang, Cédric Demonceaux, Radu Timofte, and Luc Van Gool. 2022. Source-free Depth for Object Pop-out. *arXiv preprint arXiv:2212.05370* (2022).
- [65] Zhenyu Wu, Lin Wang, Wei Wang, Tengfei Shi, Chenglizhao Chen, Aimin Hao, and Shuo Li. 2022. Synthetic data supervised salient object detection. In *ACM MM*.
- [66] Zongwei WU, Zhuyun ZHOU, Guillaume Allibert, Christophe Stolz, Cédric Demonceaux, and Chao Ma. 2022. Transformer Fusion for Indoor Rgb-D Semantic Segmentation. *Available at SSRN 4251286* (2022).
- [67] Mochu Xiang, Jing Zhang, Yunqiu Lv, Aixuan Li, Yiran Zhong, and Yuchao Dai. 2021. Exploring Depth Contribution for Camouflaged Object Detection. *arXiv e-prints* (2021), arXiv–2106.
- [68] Xiaolin Xiao, Yicong Zhou, and Yue-Jiao Gong. 2019. RGB-‘D’ Saliency Detection With Pseudo Depth. *IEEE TIP* 28, 5 (2019), 2126–2139. <https://doi.org/10.1109/TIP.2018.2882156>
- [69] Zhengxuan Xie, Feng Shao, Gang Chen, Hangwei Chen, Qiuping Jiang, Xiangchao Meng, and Yo-Sung Ho. 2023. Cross-Modality Double Bidirectional Interaction and Fusion Network for RGB-T Salient Object Detection. *IEEE TCSVT* (2023).
- [70] Senbo Yan, Liang Peng, Chuer Yu, Zheng Yang, Haifeng Liu, and Deng Cai. 2022. Domain Reconstruction and Resampling for Robust Salient Object Detection. In *ACM MM*.
- [71] Maoke Yang, Kun Yu, Chi Zhang, Zhiwei Li, and Kuiyuan Yang. 2018. Denseaspp for semantic segmentation in street scenes. In *IEEE CVPR*.
- [72] Zongxin Yang, Linchao Zhu, Yu Wu, and Yi Yang. 2020. Gated channel transformation for visual recognition. In *IEEE/CVF CVPR*.
- [73] Bowen Yin, Xuying Zhang, Qibin Hou, Bo-Yuan Sun, Deng-Ping Fan, and Luc Van Gool. 2022. CamoFormer: Masked Separable Attention for Camouflaged Object Detection. *arXiv preprint arXiv:2212.06570* (2022).
- [74] Chen Zhang, Runmin Cong, Qinwei Lin, Lin Ma, Feng Li, Yao Zhao, and Sam Kwong. 2021. Cross-modality discrepant interaction network for RGB-D salient object detection. In *ACM MM*.
- [75] Chen Zhang, Runmin Cong, Qinwei Lin, Lin Ma, Feng Li, Yao Zhao, and Sam Kwong. 2021. Cross-modality Discrepant Interaction Network for RGB-D Salient Object Detection. In *ACM MM*.
- [76] Jing Zhang, Deng-Ping Fan, Yuchao Dai, Xin Yu, Yiran Zhong, Nick Barnes, and Ling Shao. 2021. RGB-D Saliency Detection via Cascaded Mutual Information Minimization. In *IEEE ICCV*.
- [77] Miao Zhang, Shuang Xu, Yongri Piao, Dongxiang Shi, Shusen Lin, and Huchuan Lu. 2022. PreyNet: Preying on Camouflaged Objects. In *ACM MM*.
- [78] Miao Zhang, Shunyu Yao, Beiqi Hu, Yongri Piao, and Wei Ji. 2022. C2DFNet: Criss-Cross Dynamic Filter Network for RGB-D Salient Object Detection. *IEEE TMM* (2022).
- [79] Qiang Zhang, Tonglin Xiao, Nianchang Huang, Dingwen Zhang, and Jungong Han. 2020. Revisiting feature fusion for RGB-T salient object detection. *IEEE TCSVT* 31, 5 (2020), 1804–1818.
- [80] Wenbo Zhang, Ge-Peng Ji, Zhuo Wang, Keren Fu, and Qijun Zhao. 2021. Depth Quality-Inspired Feature Manipulation for Efficient RGB-D Salient Object Detection. In *ACM MM*.
- [81] Hengshuang Zhao, Jianping Shi, Xiaojuan Qi, Xiaogang Wang, and Jiaya Jia. 2017. Pyramid scene parsing network. In *IEEE CVPR*.
- [82] Jiawei Zhao, Yifan Zhao, Jia Li, and Xiaowu Chen. 2020. Is depth really necessary for salient object detection?. In *ACM MM*.
- [83] Yifan Zhao, Jiawei Zhao, Jia Li, and Xiaowu Chen. 2021. RGB-D salient object detection with ubiquitous target awareness. *IEEE TIP* 30 (2021), 7717–7731.
- [84] Jiayuan Zhou, Lijun Wang, Huchuan Lu, Kaining Huang, Xinchu Shi, and Bocong Liu. 2022. MVSsalNet: Multi-view Augmentation for RGB-D Salient Object Detection. In *ECCV*.
- [85] Tao Zhou, Huazhu Fu, Geng Chen, Yi Zhou, Deng-Ping Fan, and Ling Shao. 2021. Specificity-preserving RGB-D Saliency Detection. In *IEEE ICCV*.
- [86] Wujie Zhou, Qinling Guo, Jingsheng Lei, Lu Yu, and Jenq-Neng Hwang. 2021. ECFFNet: Effective and consistent feature fusion network for RGB-T salient object detection. *IEEE TCSVT* 32, 3 (2021), 1224–1235.
- [87] Wujie Zhou, Yun Zhu, Jingsheng Lei, Jian Wan, and Lu Yu. 2021. APNet: Adversarial learning assistance and perceived importance fusion network for all-day RGB-T salient object detection. *IEEE TETCI* 6, 4 (2021), 957–968.
- [88] Wujie Zhou, Yun Zhu, Jingsheng Lei, Rongwang Yang, and Lu Yu. 2023. LSNet: Lightweight spatial boosting network for detecting salient objects in RGB-thermal images. *IEEE TIP* 32 (2023), 1329–1340.